

Rotational Pixel Swapping Method for Detection of Circular Features in Binary Images

Satoru Yamamoto, Tsuneo Matsunaga, Ryosuke Nakamura, Yasuhito Sekine, Naru Hirata, and Yasushi Yamaguchi, *Member, IEEE*

Abstract—We propose a new automatic method called the rotational pixel swapping (RPSW) method to detect circular features in binary images of remote sensing images. The method is based on a multiplication operation between the original image and the rotated images. We show that the RPSW selectively enhances rotational symmetric patterns and weakens nonrotational symmetric patterns, including noise components, without any noise reduction processes. The method can detect not only simple circles but also more complex circular features such as incomplete ring structures or several concentric rings. Furthermore, we demonstrate that the RPSW provides the stable detection of circular features such as terrestrial impact structures, which are irregular imperfect circular shapes, in binary images based on Earth-observation satellite images. The RPSW would provide a potential method of future surveys or statistical studies using huge data sets of multiband or hyperspectral images obtained by Earth-observation satellites.

Index Terms—Feature extraction, object detection, remote sensing.

I. INTRODUCTION

RECENT progress in remote sensing techniques has provided huge data sets of remote sensing images. Various circular features, such as impact craters, volcanoes, geological domes, and man-made structures/symbols, are found in terrestrial images. There would exist small circular features which have not been recognized on the Earth. For example, Folco *et al.* [1] discovered a potential impact crater (the Kamil crater) in Egypt. This crater was identified in Google Earth, and a later field study confirmed as an impact origin. Although their findings may be somewhat serendipity, this indicates that more potential craters are expected to be found from terrestrial remote sensing data. In order to find unrecognized circular features such as potential impact craters from terrestrial remote sensing data, a survey study for circular features using the

huge number of remote sensing images is needed. Thus, an automated technique for detecting circular features from remote sensing images would help in the utilization of the huge number of remote sensing images.

Various techniques for automatic extraction of impact craters as well as geological features have been developed based on the pattern-matched filtering technique or Hough transform [2]–[13]. These previous studies are appropriate for targeting areas where circular impact craters are dominant over non-circular geologic features, such as on Mars, the Moon, and asteroids. On the other hand, when we apply these techniques to Earth-observation satellite images, where noncircular features are dominant, we need various preprocesses to remove non-circular features from an image. For example, in several trials using the Hough transform to detect circular features in Earth-observation satellite images, many mathematical morphology operators are required before the Hough transform can be applied [4]. This significantly increases the calculation time. This is not appropriate for surveys or statistical studies using huge data sets of remote sensing images.

In this paper, we propose a new method for automated detection and extraction of circular features in black-and-white images (1-b binary images) based on Earth-observation satellite images. The method is partly based on pixel swapping (PSW) for extraction of particular patterns in [14]. Although there are various multiband or hyperspectral images obtained by Earth-observation satellites, the current version of this method can handle only binary images. However, in order to obtain a sophisticated algorithm for full automated detection and extraction using the multiband or hyperspectral images, it is important to fully examine a basic algorithm for detection and extraction for binary images. Thus, in this study, we focus on the detectability of our proposed method that treats only binary images, as well as the parameter studies. We demonstrate how this new method can detect circular features from several binary images that also include varied noncircular features, which are based on remote sensing images obtained by the Advanced Spaceborne Thermal Emission and Reflection Radiometer (ASTER) on board the Terra satellite [15]–[17].

II. METHOD

A. Basic Idea: PSW

The PSW [14] extracts particular patterns by performing an interpicture operation between an original image and its translational operation image. In this method, a target pattern in the “shift table,” as it is called in the original paper, is used

Manuscript received October 28, 2013; revised March 10, 2014 and May 1, 2014; accepted May 23, 2014.

S. Yamamoto and T. Matsunaga are with the Center for Environmental Measurement and Analysis, National Institute for Environmental Studies, Tsukuba, 305-8506, Japan (e-mail: yamamoto.satoru@nies.go.jp).

R. Nakamura is with the Information Technology Research Institute, National Institute of Advanced Industrial Science and Technology, Tsukuba 305-8568, Japan.

Y. Sekine is with the Department of Complexity Science and Engineering, University of Tokyo, Kashiwa 277-8561, Japan.

N. Hirata is with the Aizu Research Cluster for Space Science, Research Center for Advanced Information Science and Technology, The University of Aizu, Aizu-Wakamatsu 965-8580, Japan.

Y. Yamaguchi is with the Graduate School of Environmental Studies, Nagoya University, Nagoya 464-8601, Japan.

Color versions of one or more of the figures in this paper are available online at <http://ieeexplore.ieee.org>.

Digital Object Identifier 10.1109/TGRS.2014.2327121

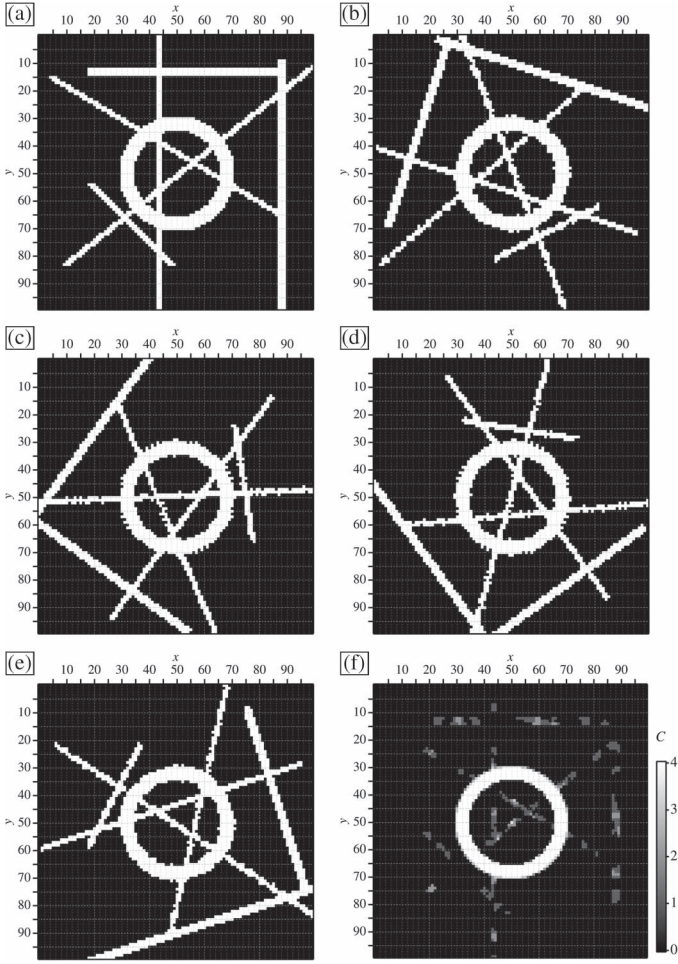


Fig. 1. (a) Target image of A for $L \times L = 100 \times 100$ pixels. (b)–(e) Rotated images of B with (b) $\phi = 72^\circ$, (c) $\phi = 144^\circ$, (d) $\phi = 216^\circ$, and (e) $\phi = 288^\circ$, respectively. (f) Extracted image of C from the (a)–(e) images.

as the rule of the translational operation. Although the PSW can extract not only the exact same pattern but also a similar pattern to that in the shift table, only a pattern of similar size to that in the shift table can be extracted. Therefore, if we try to extract circular features by the PSW, we must prepare all possible sizes of patterns for the shift table. In addition, when we try to detect several concentric rings as a circular feature, we must prepare all combinations of the shapes in the shift table: the number of rings, radius of each ring, and the widths. This is not computationally feasible.

Note that circular and concentric ring features are a rotational symmetric pattern (RSP), whereas the PSW uses a translational operation. Thus, we propose a rotational operation rather than a translational operation. In this case, we do not need to use the shift table. In the following, we explain how the introduction of a rotational operation can detect circular features without the shift table. We call this advanced method “rotational PSW” (RPSW).

B. RPSW

The RPSW extracts an RSP by multiplication operations between the original image and the rotated images. We explain the essence of the RPSW by using the sample image $A(x, y)$ in Fig. 1(a), which is a black-and-white image (that

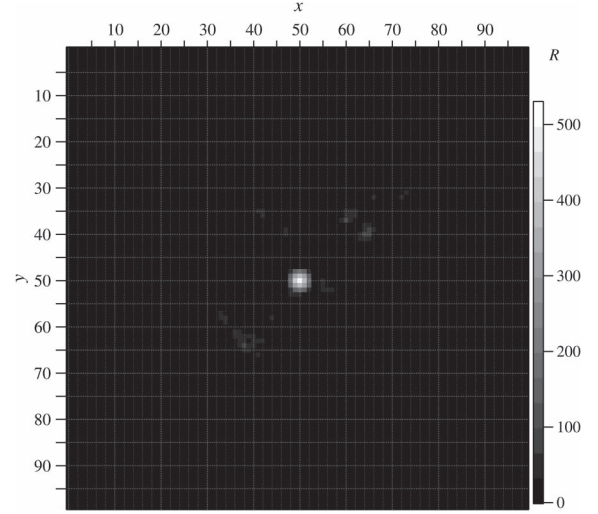


Fig. 2. Contour map of $R(x, y)$ for Fig. 1(a) with $\Delta\phi = 72^\circ$. The lighter colors indicate higher R values.

is, $A(x, y) = 1$ (white) or 0 (black)) with dimensions $L \times L = 100 \times 100$ pixels. In this paper, we define the x - and y -axes as the horizontal and vertical axes in an image, respectively. We also define the top-left point in the image as $(x = 0, y = 0)$. From Fig. 1(a), we produced rotated images of $B_{x_n, y_n, \phi}(x, y)$ for the rotation angles $\phi = 72^\circ$ [Fig. 1(b)], $\phi = 144^\circ$ [Fig. 1(c)], $\phi = 216^\circ$ [Fig. 1(d)], and $\phi = 288^\circ$ [Fig. 1(e)] with the rotation center at $(x_n = 50, y_n = 50)$. Then, we calculated multiplication $M_\phi(x, y) = A(x, y) \cdot B_{x_n, y_n, \phi}(x, y)$ for each ϕ and then summed over $M_\phi(x, y)$ for all ϕ to produce the extracted image C in Fig. 1(f). We can see that the circular feature (a ring pattern) is enhanced, while the lines and rectangles in Fig. 1(a) are weakened or eliminated.

To search for the center of an RSP (hereinafter, CRSP) in a target image, we used the following rotational symmetricalness function:

$$R(x, y) = \sum_i \sum_j \prod_{k=0}^N B_{x, y, \phi=k \cdot \Delta\phi}(i, j) \quad (1)$$

where (x, y) is the rotation center for the calculation of the rotated image $B_{x, y, \phi}$, $\Delta\phi$ is an incremental angle of rotation, and N is the total number of rotation images. If the rotation center (x, y) is near the CRSP, R is large. In contrast, if the rotation center is far from the CRSP, R is small. Thus, a relatively high R value at a point indicates that the point is the center of a circular feature, i.e., CRSP. Fig. 2 shows the $R(x, y)$ calculated for Fig. 1(a), where we used $\Delta\phi = 72^\circ$. We found that the point at (50, 50) exhibits the maximum peak value of $R = 534$, while most of the pixels far from the point at (50, 50) show $R = 0$. The point at (50, 50) corresponds to the center of the ring seen in Fig. 1(a).

In practical implementation for the calculation of R , we first generated the N rotation images by $\Delta\phi$ around the image center and then shifted them to the location needed for different centers of the rotation. In most cases of an arbitrary rotational angle, the rotated image does not fit into a bounding box of the original image. We assumed the values of zero for all other pixels outside the original bounding box and performed

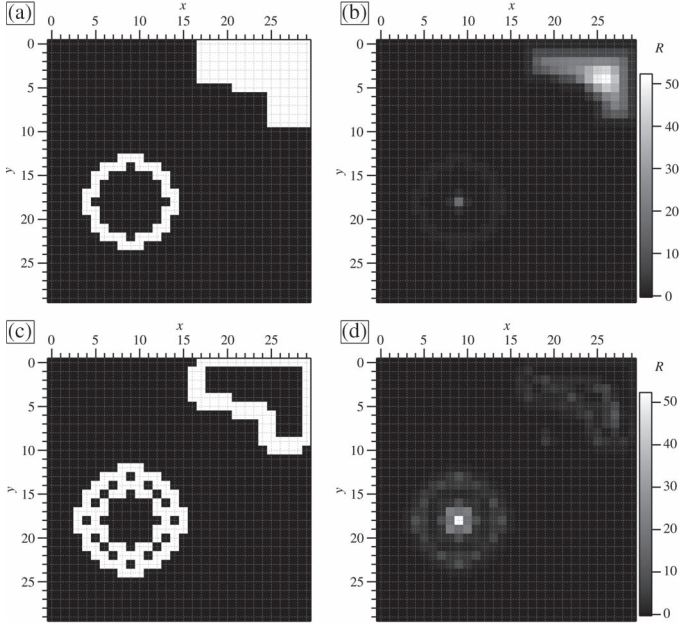


Fig. 3. (a) Target image that has a ring feature and the filled area at the corner. Dimensions of the image are $L \times L = 30 \times 30$ pixels. (b) Contour map of R for (a) with $\Delta\phi = 120^\circ$. (c) Edge image for (a). (d) Contour map of R for (c) with $\Delta\phi = 120^\circ$.

the multiplication of images within the bounding box. We calculated $R(x, y)$ only for the following region (i, j) :

$$l_{\min} < \sqrt{(i-x)^2 + (j-y)^2} < l_{\max} \quad (2)$$

where l_{\max} and l_{\min} are the maximum and minimum local RPSW radii, respectively. The use of l_{\max} and l_{\min} is mainly for reducing the processing time T for R . The introduction of these to a target image of $L \times L$ pixels reduces the processing time to $\sim T_{\text{all}} \cdot \pi(l_{\max}^2 - l_{\min}^2)/L^2$, where T_{all} is the calculation time for all pixels. The l_{\max} also means that we set the upper limit of the size (e.g., $2l_{\max}$) of the circular feature for a target. The l_{\min} is used mostly to save computation time by not bothering to check for tiny little noiselike features. In addition, we calculated $R(x, y)$ every s pixel in both directions (we call s the survey step). For example, we calculate $R(x, y)$ for all pixels for $s = 1$, while we calculate $R(x, y)$ for every other x and y for $s = 2$. The introduction of s reduces the processing time to T_{all}/s^2 . The survey step is used only for the calculation of R , not C .

The extraction process is as follows: For multiple detection of RSPs, we selected all points (x_n, y_n) whose R values are higher than a threshold value of $f \cdot R_{\max}$, where f is the threshold fraction and R_{\max} is the maximum value in R . We then calculated $C_n(x, y)$ for (x_n, y_n) for each RSP whose R value is the n th highest in R as

$$C_n(x, y) = \sum_{k=1}^N A(x, y) \cdot B_{x_n, y_n, \phi=k \cdot \Delta\phi}(x, y). \quad (3)$$

We calculated $C_n(x, y)$ only for the region (i, j) defined by (2) and then summed up all $C_n(x, y)$ for the RSPs with $R > f \cdot R_{\max}$, i.e., $C(x, y) = \sum_n C_n(x, y)$.

Note that the RPSW extracts a filled area as an RSP. Fig. 3(a) is an example image that has a ring feature and a filled area.

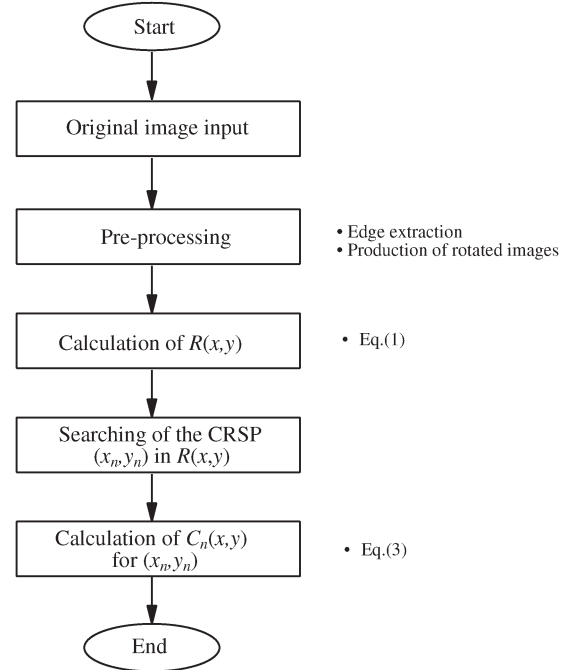


Fig. 4. Flowchart of the RPSW.

TABLE I
PARAMETERS FOR THE RPSW

Parameter	Definition
$\Delta\phi$	Incremental angle
l_{\max} and l_{\min}	Maximum and minimum local RPSW radii
s	Survey step
f	Threshold fraction

When we calculate R for Fig. 3(a) with $\Delta\phi = 120^\circ$, $s = 1$, $l_{\max} = 30$, and $l_{\min} = 0$, we find that many points with higher R values ($R > 20$) exist at the top-right corner, as shown in Fig. 3(b). On the other hand, the center of the ring feature at (9, 18) is $R = 16$, which is smaller than those at the top-right corner. In this case, the filled area at the top-right corner is mistakenly extracted as RSPs. To avoid the mistaken extraction of the filled area, we used edge extraction as preprocessing in the RPSW. Fig. 3(c) shows the edge image derived from Fig. 3(a) after the Sobel operation (SO), where we set $A(x, y) = 1$ for the pixel at (x, y) whose gradient magnitude (i.e., the combination of horizontal and vertical derivative approximations) after the SO is equal to or larger than one. Then, we calculated R for the edge image by using the same parameters as Fig. 3(b), as shown in Fig. 3(d). In this case, we can see that the maximum value is located at (9, 18) with $R = 52$, which corresponds to the center of the ring feature in Fig. 3(a). On the other hand, we do not see any points with $R > 10$ in the top-right corner. We thus conclude that edge extraction should be applied as preprocessing prior to the RPSW. In the following, we use the SO as the preprocessing (we will discuss how the results depend on an operation used for the edge extraction in Section V-A).

Fig. 4 shows a flowchart of the RPSW, and the parameters used for the RPSW are summarized in Table I.

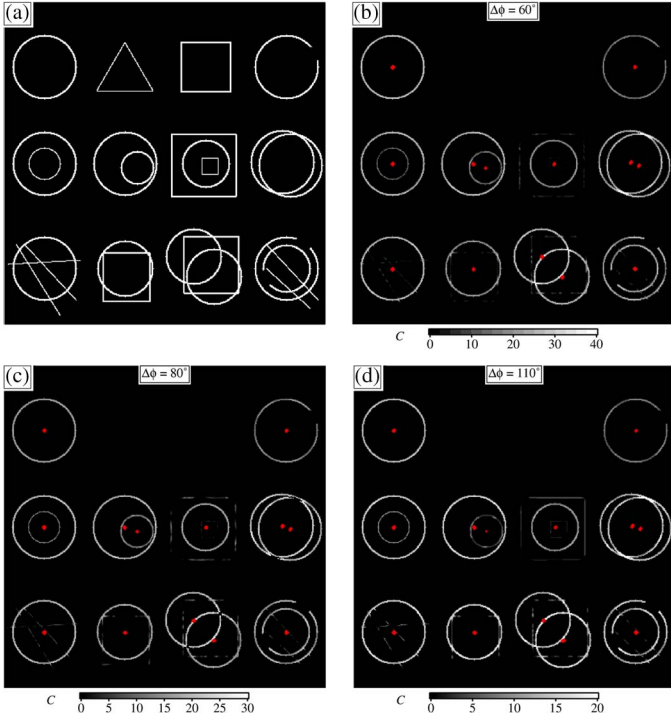


Fig. 5. (a) Artificial pattern of dimensions $L \times L = 400 \times 400$ pixels. (b) Extracted image $C(x, y)$ with the CRSPs as red points for $\Delta\phi = 60^\circ$ ($N = 5$). (c) Same as (b) but for $\Delta\phi = 80^\circ$ ($N = 4$). (d) Same as (b) but for $\Delta\phi = 110^\circ$ ($N = 3$).

III. RESULTS: ARTIFICIAL PATTERN

A. Simple Circular Pattern

We first tried to detect the artificial circular pattern shown in Fig. 5(a), which is a black-and-white image of dimensions $L \times L = 400 \times 400$ pixels. In this target image, we prepared 12 sample shapes. The top row has four shapes: a circle, a triangle, a rectangle, and an imperfect circle. The middle row has several combinations of shapes: concentric circles, nonconcentric circles, a circle sandwiched between two rectangles, and two overlapping circles. The bottom row has circles overlapped with lines or rectangles.

We applied the RPSW to Fig. 5(a). The parameters used are summarized in Table II. Fig. 5(b) shows the extracted image $C(x, y)$ for $\Delta\phi = 60^\circ$, which is the sum of $C_n(x, y)$ for each CRSP (red point). In the top row, we can see that the circle and the imperfect circle are successfully extracted. On the other hand, the triangle and rectangle in the second and third columns are not extracted, because they are not regarded as an RSP under the condition $\Delta\phi = 60^\circ$. In the middle row, all circular shapes are extracted. In the third column, the circles are extracted, while the rectangles are eliminated or weakened significantly. Even two overlapping circles in the fourth column are clearly extracted. In the bottom row, we also see that every circle is extracted, while the lines and rectangles are eliminated or weakened significantly. We also examined the cases of $\Delta\phi = 80^\circ$ [Fig. 5(c)] and $\Delta\phi = 110^\circ$ [Fig. 5(d)]. There is no clear difference in the extracted images among $\Delta\phi = 60^\circ$, 80° , and 110° , suggesting that we do not need to choose $\Delta\phi$ to permit the full rotation through a figure back

to the starting point. Although the noncircular features such as rectangles or lines for $\Delta\phi = 60^\circ$ seem to be weakened more significantly than those for $\Delta\phi = 80^\circ$ or $\Delta\phi = 110^\circ$, this is due to the larger N for $\Delta\phi = 60^\circ$ ($N = 5$) than those for $\Delta\phi = 80^\circ$ ($N = 4$) and $\Delta\phi = 110^\circ$ ($N = 3$). The increase in N would increase the contrast between the RSPs and non-RSPs.

Note that we used a single set of the parameters, shown in Table II, for Fig. 5. In other words, although we do not optimize the parameters for individual shapes in the target image, we can simultaneously extract only the circular features from Fig. 5(a). Thus, we do not need individual parameter selections for each shape in a target image.

B. Multiple Circular Pattern

We next tried to detect the artificial overlapping circles having power-law size distribution shown in Fig. 6(a), which is a black-and-white image of dimensions $L \times L = 500 \times 500$ pixels. In this target image, we prepared 45 circles with radii ranging from 10 to 100 pixels, whose cumulative size distribution is assumed to be power law with exponent of -1.8 [18]. We applied the RPSW to Fig. 6(a). The parameters used are summarized in Table II. Fig. 6(b) shows the extracted image $C(x, y)$ for $\Delta\phi = 60^\circ$, which is the sum of $C_n(x, y)$ for each CRSP (red point). All centers of the circles are successfully detected by the RPSW, although we can also see several false detections outside the circles. However, when we applied the RPSW with $\Delta\phi = 51.4^\circ$ to Fig. 6(a), there are no false detections, and all centers of the circles are successfully detected.

C. Detectable Circularity

The RPSW can detect a ring-shaped feature whose minor axis radius b is

$$b \geq a - \Delta w \quad (4)$$

where a is the major axis radius and Δw is the width of the boundary of the feature (e.g., $\Delta w = 3$ for the SO for a ring with a width of $w = 1$). From (4), we expect that a circular feature with a larger Δw could be detected even for a smaller circularity ($\beta = b/a$) by the RPSW. In Fig. 7, we demonstrated how ellipsoidal shapes with certain widths can be detected by the RPSW. In this figure, we prepared 16 ellipses with $a = 45$ pixels; β is different by column, where the values of β are 0.95, 0.92, 0.90, and 0.87 from left to right; w is different by row, where the values of w are 1, 2, 3, and 4 from top to bottom. Fig. 7(b) shows the extracted image by the RPSW with parameters in Table II. For the case of $w = 1$ (the first row), only the ellipse with $\beta = 0.95$ is detected. However, for the case of $w = 2$ (the second row), the two ellipses with $\beta = 0.95$ and 0.92 are detected, and for the case of $w = 3$ (the third row), the three ellipses with $\beta = 0.95$, 0.92, and 0.90 are detected. In the bottom row, we can see that all ellipses are detected. Thus, it is shown that the increase in w increases the detectability of ellipses with smaller β . From (4), the critical detectable β_d for $a = 45$ pixels are $\beta_d \sim 0.933$ ($w = 1$), 0.911 ($w = 2$), 0.888 ($w = 3$), and 0.867 ($w = 4$), where we

TABLE II
PARAMETERS USED IN THE RPSW

	Fig. 5	Fig. 6	Fig. 7	Figs. 9–11	Figs. 12 and 13	Fig. 14	Fig. 15	Fig. 17
Target	Artificial	Artificial	Artificial	GB, TB, and BP	GB, TB, and BP	GB, TB, and BP	GB, TB, and BP	Artificial
$L \times L$	400×400	500×500	400×400	600×600	600×600	600×600	600×600	500×500
$\Delta\phi$	$60^\circ, 80^\circ, \text{ or } 110^\circ$	$51.4^\circ \text{ or } 60^\circ$	60°	60°	variable	60°	60°	60°
l_{\max}	50 px	100 px	50 px	100 px	100 px	100 px	100 px	100 px
l_{\min}	0 px	10 px	0 px	20 px	20 px	20 px	20 px	20 px
f	0.2	0.1	0.2	0.7 and 0.9	0.9	0.9	0.9	0.9
s	1	1	1	1 and 5	1	variable	5	2

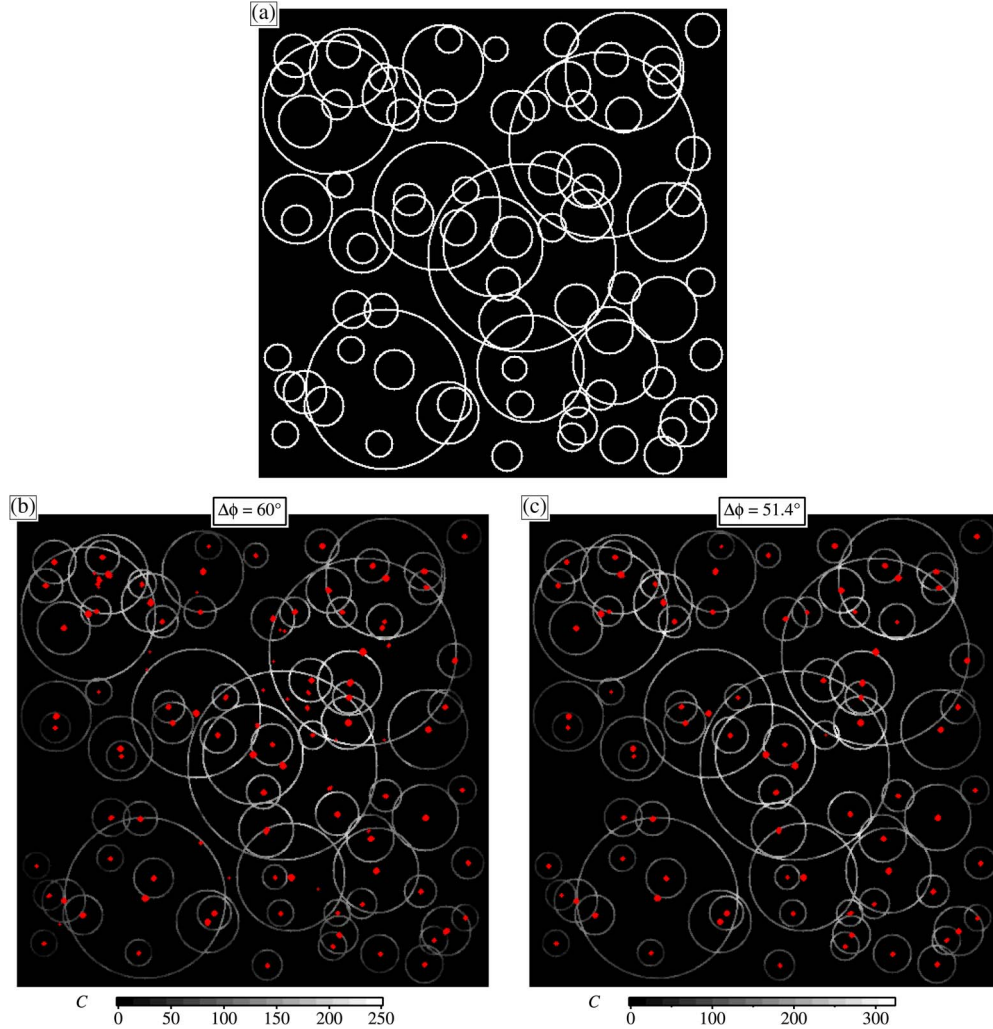


Fig. 6. (a) Artificial pattern of overlapping circles having power-law size distribution ($L \times L = 500 \times 500$ pixels). (b) Extracted image by the RPSW for (a) with $\Delta\phi = 60^\circ$. (c) Extracted image by the RPSW for (a) with $\Delta\phi = 51.4^\circ$.

assumed that $\Delta w = w + 2$. Thus, the values of β_d derived from (4) are consistent with the results in Fig. 7(b).

Since the detectability of the RPSW depends on the width of the ring, a morphological operation that expands the width such as a line thickening operation would improve the detectability of the RPSW. The increase in the width of the ring by the line thickening operation also increases the detectability of ellipses with smaller β . Although this would help the RPSW for ellipses with smaller β , the current version of the RPSW does not use the line thickening operation as preprocessing.

IV. APPLICATION TO REMOTE SENSING IMAGES

A. Target Image

We next applied the RPSW to the geological circular features in ASTER images. Here, we prepared three terrestrial impact structures as a target in remote sensing image: Gosses Bluff (GB) in Australia [Fig. 8(a)], Tin Bider (TB) in Algeria [Fig. 8(b)], and B.P. Structure (BP) located in the Sahara desert in Libya [Fig. 8(c)]. These impact structures show the circular features that have different colors from the surroundings in the

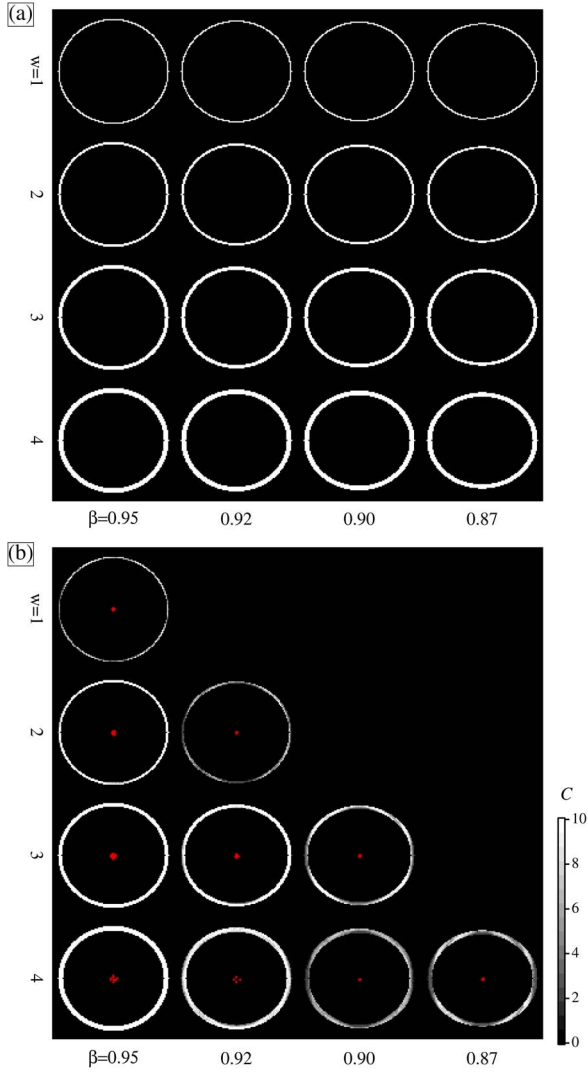


Fig. 7. (a) Artificial patterns of ellipses with $a = 45$ pixels and various circularities β and widths w ($L \times L = 400 \times 400$ pixels). The β is different by column, where the values of β are 0.95, 0.92, 0.90, and 0.87 from left to right. The w is different by row, where the values of w are 1, 2, 3, and 4 from top to bottom. (b) Extracted image by the RPSW for (a). The CRSPs are shown as red “+” symbols.

color composite images. The circular feature with a different color corresponds to the impact structure (i.e., central peaks and peak rings of an impact crater). However, the distinct color is not due to the material alternations by impact shocked processes. This is due to the difference in reflectance spectra between the uplifted materials and the surroundings. During the impact processes, the deeper layers of the materials are uplifted by the gravitational unstable, forming the central peaks or rings [18], [19]. Indeed, for these impact craters, the geological formations of the impact structures are different from those of the uppermost layer of the surface [20]–[24]. The difference in the geological formations between the surface and the deeper layers can produce the circular features with distinct color from the surroundings. Therefore, the circular features with distinct color for terrestrial impact structures in multiband images depend on the regional geological setting.

In this section, we attempted to extract the circular features that have different colors by the RPSW. However, since the

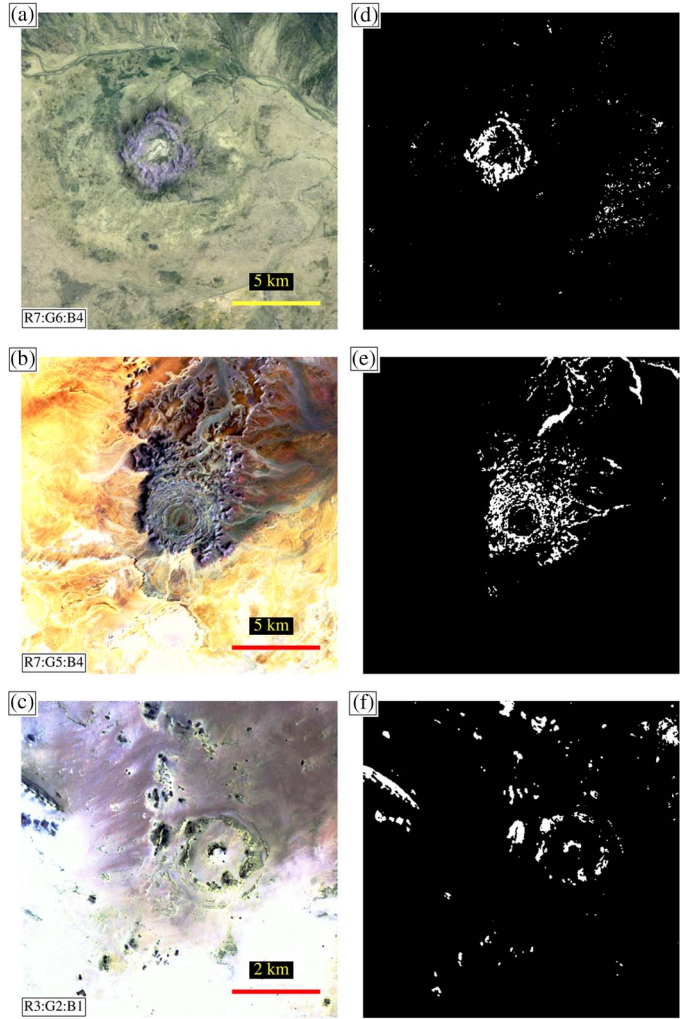


Fig. 8. (a) ASTER color composite images ($L \times L = 600 \times 600$) for the terrestrial impact structures: (a) GB, (b) TB, and (c) BP (red, green, and blue are assigned to the bands of $n = 7$, 6, and 4 for (a), $n = 7$, 5, and 4 for (b), and $n = 3$, 2, and 1 for (c), respectively). (d) Binarized image for (a). (e) Binarized image for (b). (f) Binarized image for (c).

current version of the RPSW can handle only binary images, we need to binarize the multiband image of these impact structures before applying the RPSW. In this case, image classification processes such as spectral pattern recognition are needed. Since, in this paper, we focus on the detectability of the circular features in binary images by the RPSW, we do not try to combine the image classification processes into the RPSW. Alternatively, we manually binarized the images to emphasize the circular features with distinct colors for these three targets. Then, we examined how the RPSW can extract the circular features from the binary images.

The band selection procedure to produce the binarized image is as follows: For the case of the GB, we selected pixels with $r_4 > \mu_4 + \sigma_4$ as well as $r_7 < \mu_7 + \sigma_7$, where r_n is the reflectance at band n , and μ_n and σ_n are the average reflectance and standard deviation of r_n , respectively (bands $n = 4$ and 7 correspond to wavelengths $\lambda = 1.600\text{--}1.700 \mu\text{m}$ and $\lambda = 2.235\text{--}2.285 \mu\text{m}$, respectively). We can see a rhombus feature in Fig. 8(d), which corresponds to the central uplift of the GB. For the case of the TB, we selected pixels with $r_4 < \mu_4 - 0.4\sigma_4$ as well as $r_7 < \mu_7 - 0.8\sigma_7$, producing the binary image in

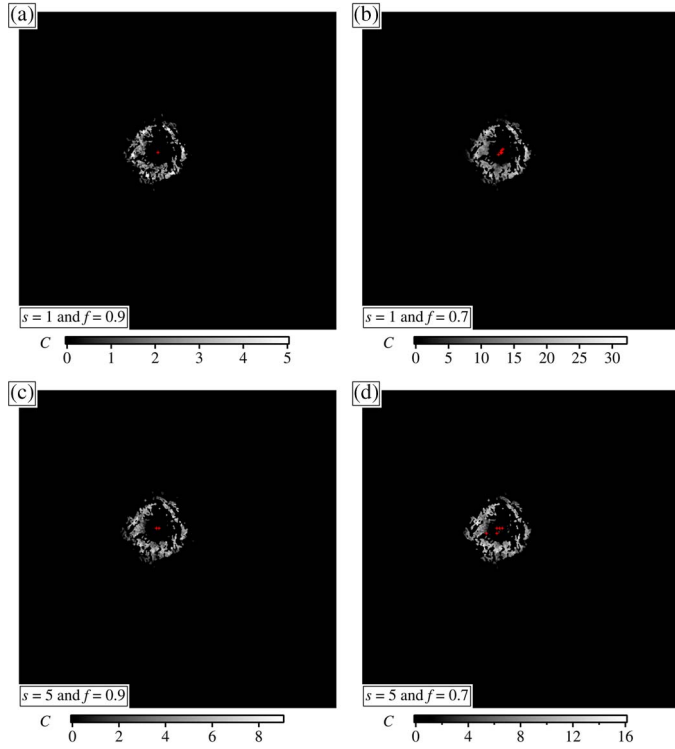


Fig. 9. Extracted image $C(x, y)$ for the GB for (a) $s = 1$ and $f = 0.9$, (b) $s = 1$ and $f = 0.7$, (c) $s = 5$ and $f = 0.9$, and (d) $s = 5$ and $f = 0.7$ with scale bars for C value. The CRSPs are shown as red “+” symbols. The values of the total number of CRSPs are (a) one, (b) seven, (c) two, and (d) five, respectively.

Fig. 8(e). We can see a circular feature with a wide width surrounded by noncircular features and noise. For the BP, we selected pixels with $r_3 < \sim \mu_3 - 2\sigma_3$ ($\lambda = 0.76\text{--}0.86 \mu\text{m}$), producing the binarized image in Fig. 8(f). We see the ring structure with several parts missing due to erosion or sand coverage (hereinafter, broken ring structure).

B. GB

We applied the RPSW to the binarized image for the GB [Fig. 8(d)] with the parameters in Table II. Fig. 9(a) shows the extracted image $C(x, y)$ for $s = 1$ and $f = 0.9$, where we can see a rhombus feature, which corresponds to the central uplift of the GB [Fig. 8(a)]. The CRSPs shown by the red “+” symbol are located at the center of the central uplift of the GB. On the other hand, the noise components in Fig. 8(d) are not seen in the extracted image. Thus, in spite of its irregular shape, we succeeded in the detection of the central uplift of the GB as a geological circular feature. Fig. 9(b) shows the result for $f = 0.7$ ($s = 1$), where the total number of CRSPs is seven, which is larger than one for $f = 0.9$. However, the extracted image for $f = 0.7$ shows a circular feature similar to that for $f = 0.90$. Although several CRSPs for $f = 0.7$ seem to be slightly offset from the center of the GB, the calculation of C_n selectively enhances the RSP, while the non-RSP components hardly contribute to C_n even for CRSPs offset from the center. We also examined the case of $f = 0.5$, but we found a similar

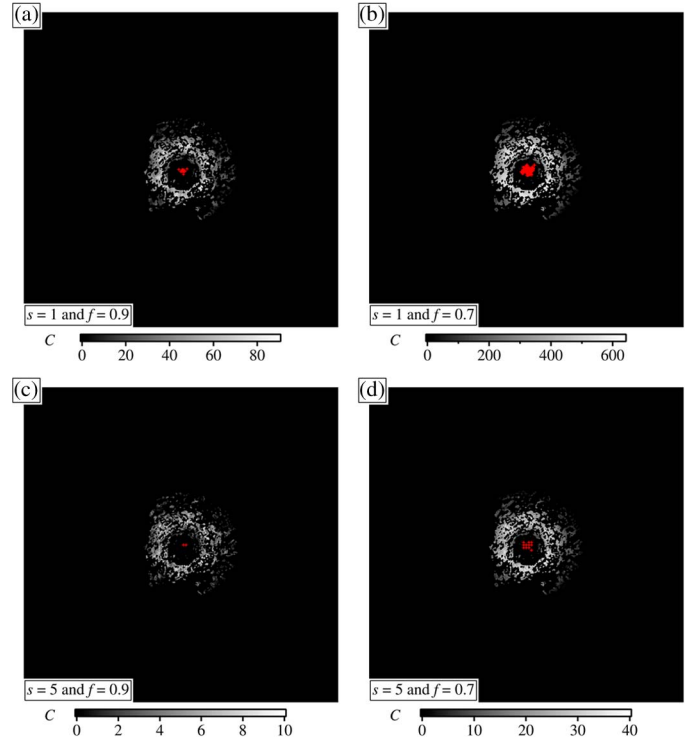


Fig. 10. Extracted image $C(x, y)$ for the TB for (a) $s = 1$ and $f = 0.9$, (b) $s = 1$ and $f = 0.7$, (c) $s = 5$ and $f = 0.9$, and (d) $s = 5$ and $f = 0.7$ with scale bars for C value. The CRSPs are shown as red “+” symbols. The values of the total number of CRSPs are (a) 21, (b) 198, (c) 2, and (d) 11, respectively.

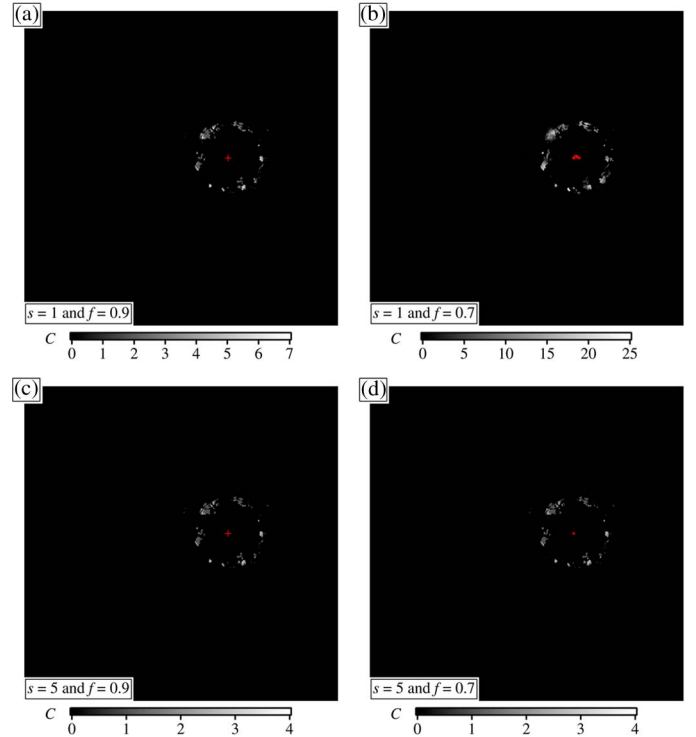


Fig. 11. Extracted image $C(x, y)$ for the BP for (a) $s = 1$ and $f = 0.9$, (b) $s = 1$ and $f = 0.7$, (c) $s = 5$ and $f = 0.9$, and (d) $s = 5$ and $f = 0.7$ with scale bars for C value. The CRSPs are shown as red “+” symbols. The values of the total number of CRSPs are (a) two, (b) eight, (c) one, and (d) one, respectively.

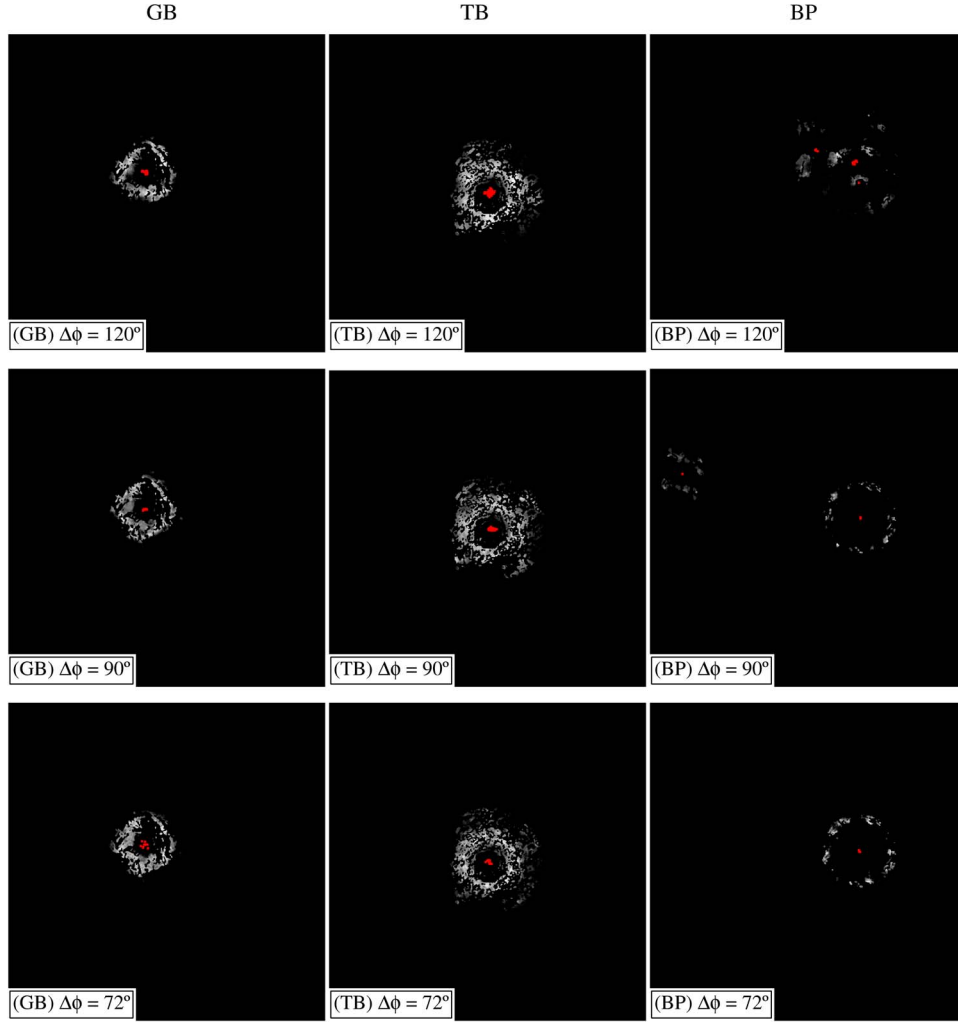


Fig. 12. Extracted images for the (left column) GB, (middle column) TB, and (right column) BP for $\Delta\phi = 120^\circ$, 90° , and 72° ($s = 1$ and $f = 0.9$). The CRSPs are plotted as “+” symbols. Here, we do not show each scale bar for C to avoid the difficulty in seeing.

extracted image to those for $f = 0.7$ and $f = 0.9$, although the total number of CRSPs increases. Thus, the extracted image hardly depends on f .

Fig. 9(c) and (d) shows the results for $s = 5$ ($f = 0.9$ and 0.7). The CRSPs are sparsely distributed as compared to those for $s = 1$, but the extracted images for $s = 5$ are similar to those for $s = 1$. Note that, for the case of $f = 0.9$, the total number of CRSPs for $s = 1$ is only one [Fig. 9(a)], while the total number for $s = 5$ is two [Fig. 9(c)]. The RPSW for $s = 5$ does not detect at the point at (263, 265) with $R = 130$, which is detected as a CRSP when $s = 1$. Alternatively, the RPSW for $s = 5$ selects the two points at (260, 260) with $R = 55$ and (265, 260) with $R = 60$, which are located near the point at (263, 265). The sum of C_n 's for the two points results in the extracted image similar to that for $s = 1$ [Fig. 9(a)].

The calculation times T are $T = 773$ s ($f = 0.9$) and 774 s ($f = 0.7$) for $s = 1$, while $T = 31$ s ($f = 0.9$) and 32 s ($f = 0.7$) for $s = 5$, respectively, where we used a C++ program in the Mac OS X 10.9 environment (2.93-GHz 6-Core Intel Xeon) using Xcode (version 5.0.2). Thus, T depends mostly on s , not on f .

C. TB

We next applied the RPSW to the binarized image for the TB [Fig. 8(e)] with the parameters in Table II. Fig. 10(a) shows the extracted image $C(x, y)$ for $s = 1$ and $f = 0.9$, where we can see a circular feature with a wide width, which corresponds to the concentric annular ridges of the TB. It is also shown that CRSPs, as shown by the red “+” symbol, are located near the center of the TB. On the other hand, we do not see other noncircular features and noise components. Thus, the RPSW succeeded in the detection of the TB as a geological circular feature. Fig. 10(b) shows the result for $f = 0.7$, where the CRSPs are widely distributed around the center of the TB. The total number of the CRSPs for $f = 0.7$ is 198, while the number for $f = 0.9$ is 21. However, the extracted image for $f = 0.7$ in Fig. 10(b) shows a circular feature similar to that for $f = 0.9$ in Fig. 10(a), although the contrast between the RSPs and non-RSPs is larger for $f = 0.7$ than that for $f = 0.9$. This is because the calculation of C_n selectively enhances the RSPs, while the non-RSP components hardly contribute to C_n even for CRSPs offset from the center. We also examined the case of $f = 0.5$, but the extracted image is similar to those in Fig. 10. Thus, the

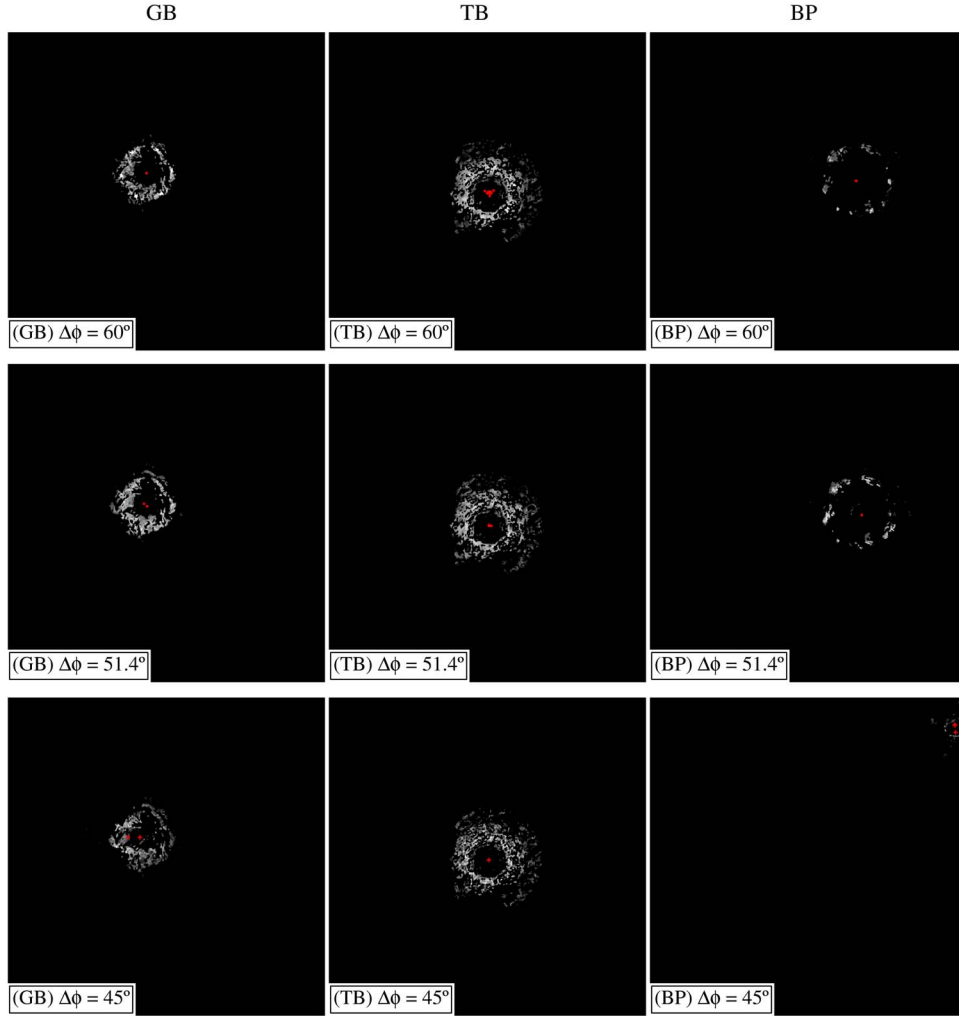


Fig. 13. Same as Fig. 12 but for $\Delta\phi = 60^\circ$, 51.4° , and 45° .

extracted image hardly depends on f , which is the same as the result for the GB.

Fig. 10(c) and (d) shows the results for $s = 5$ ($f = 0.9$ and 0.7). Although the CRSPs are sparsely distributed as compared to those for $s = 1$, the extracted images for $s = 5$ are similar to those for $s = 1$.

For the TB, $T = 779$ s ($f = 0.9$) and 791 s ($f = 0.7$) for $s = 1$, while $T = 33$ s ($f = 0.9$ and 0.7) for $s = 5$, respectively. Thus, T depends mainly on s , not on f .

D. BP

We then applied the RPSW to the binarized image for the BP [Fig. 8(f)] with the parameters in Table II. Fig. 11(a)–(d) shows the extracted images $C(x, y)$ for (a) $s = 1$ and $f = 0.9$, (b) $s = 1$ and $f = 0.7$, (c) $s = 5$ and $f = 0.9$, and (d) $s = 5$ and $f = 0.7$, respectively. We can find that all cases succeed in detection of the BP as a geological circular feature. The total numbers of CRSPs are different: (a) two, (b) eight, (c) one, and (d) one, respectively. However, there is no clear difference in the extracted image among Fig. 11(a)–(d). We also examined the case of $f = 0.5$, but the extracted images are similar to those in Fig. 11. Thus, the extracted image hardly depends on f .

For the BP, $T = 770$ s ($f = 0.9$) and 772 s ($f = 0.7$) for $s = 1$, and $T = 31$ s ($f = 0.9$) and 32 s ($f = 0.7$) for $s = 5$; T depends mainly on s , not on f .

V. DISCUSSION

Here, we discuss how the results depend on the following parameters: $\Delta\phi$, s , and the edge extraction. Then, we compare the results by the RPSW with those by Hough transform.

A. Parameter Study

1) *Incremental Angle $\Delta\phi$* : We first examined how the results depend on $\Delta\phi$. We applied the RPSW to the GB, TB, and BP in Fig. 8(d)–(f) for $\Delta\phi = 45^\circ$, 51.4° , 60° , 72° , 90° , and 120° , respectively. The results are summarized in Figs. 12 and 13, where we used the parameters in Table II. For the GB (left column in Figs. 12 and 13), all results except for $\Delta\phi = 45^\circ$ can detect the center of the circular feature that corresponds to the impact structure of the GB. For $\Delta\phi = 45^\circ$, the CRSPs are slightly offset toward the left side of the GB. In addition, the extracted feature for $\Delta\phi = 120^\circ$ shows a triangle-like pattern, which is different from that seen in Fig. 8(d). Thus, the $\Delta\phi \sim 90^\circ$ to 51.4° would be better for the GB.

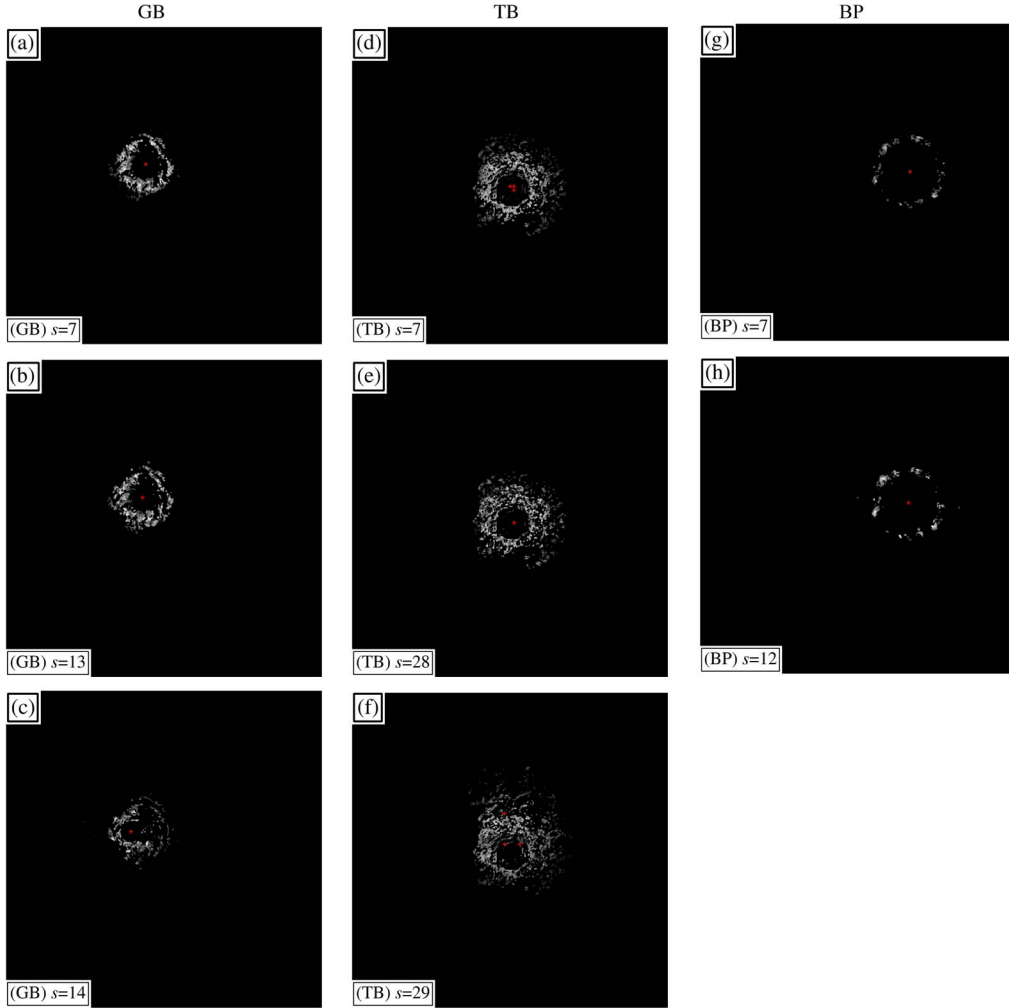


Fig. 14. Extracted images for (a)–(c) (left column) GB, (d)–(f) (middle column) TB, and [(g) and (h)] (right column) BP for various s values. Here, we use $f = 0.9$ and $\Delta\phi = 60^\circ$. The CRSPs are plotted as “+” symbols. Here, we do not show each scale bar for C to avoid the difficulty in seeing.

For the case of the TB (middle column), all CRSPs are located near the center of the circular feature that corresponds to the impact structure of the TB. For $\Delta\phi = 72^\circ$, 60° , 51.4° , and 45° , the extracted images show a circular feature with a wide width, which are similar to those in Fig. 10. However, the extracted image for $\Delta\phi = 120^\circ$ looks a triangle-like pattern. We also see a rectangle-like pattern for $\Delta\phi = 90^\circ$.

For the BP (right column), the RPSW with $\Delta\phi = 72^\circ$, 60° , and 51.4° detects the center of the BP, and the extracted images are similar to those seen in Fig. 11. On the other hand, for the case of $\Delta\phi = 90^\circ$, the RPSW detects not only the center of the BP but also the point outside the center of the BP (near left boundary of this figure). For $\Delta\phi = 120^\circ$ and 45° , the RPSW fails to detect the circular feature of the BP. Thus, for the detection of the broken circular feature like the BP, $\Delta\phi \sim 51.4^\circ - 72^\circ$ should be used.

From the aforementioned results, $\Delta\phi \sim 51.4^\circ - 72^\circ$ would be better for detection of the geological circular features in remote sensing images.

2) *Survey Step s* : We next examined how the results depend on s . We applied the RPSW to the GB, TB, and BP for various s

values, ranging from $s = 1$ to 40, where we used the parameters in Table II. Example results are plotted in Fig. 14. For the GB, the RPSW can detect the center of the GB for $s \leq 13$ [e.g., Fig. 14(a) and (b)]. However, some of the extracted images for $s \geq 14$ become distorted, because the CRSP is offset from the center of the GB [e.g., Fig. 14(c)]. For the TB, all results by the RPSW for $s \leq 28$ detect the center of the TB [e.g., Fig. 14(d) and (e)]. On the other hand, the RPSW with $s \geq 29$ fails to detect the center of the TB, resulting in the distorted extracted image, as shown in Fig. 14(f). For the BP, the RPSW for $s \leq 12$ detects well the center of the BP [Fig. 14(g) and (h)]. However, for $s \geq 13$, no CRSPs are selected, because all R values for $s \geq 13$ become zero.

In summary, the RPSW keeps the detectability for $s < 12$ or 13 for the GB and BP and for $s < 28$ for the TB. The maximum value of s for the detectability (maximum detectable s) could be related to the width of the circular feature. Indeed, the width of the circular feature for the GB and BP is roughly ~ 10 – 20 pixels, which is comparable to the maximum detectable s of $s = 12$ – 13 . In addition, the higher maximum detectable $s = 28$ for the TB could be due to its larger width of

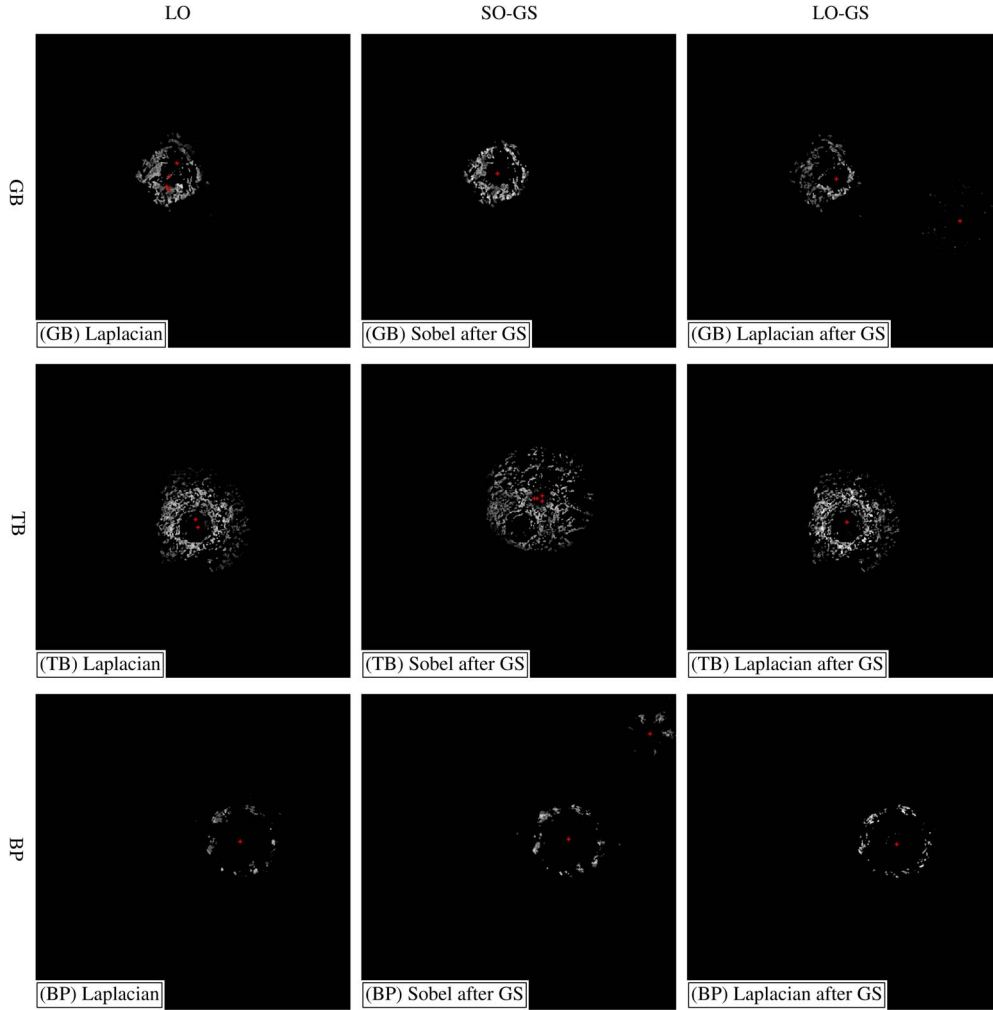


Fig. 15. Extracted images for the GB, TB, and BP for the cases of the LO, the SO-GS, and the LO-GS. Here, we use $f = 0.9$, $\Delta\phi = 60^\circ$, and $s = 5$ for all cases. The CRSPs are plotted as “+” symbols. Here, we do not show each scale bar for C' to avoid the difficulty in seeing.

the circular feature of the TB (~ 30 pixels). Thus, the maximum detectable s depends on the width of the circular feature in a target image.

3) *Edge Operation*: We also examined how the results depend on an operation used for the edge extraction. In addition to the SO as the preprocess, we also used the Laplacian operation (LO) and Gaussian smoothing (GS). Fig. 15 shows the results for the cases of the LO, SO after GS (SO-GS), and LO after GS (LO-GS), where we used the parameters in Table II. The RPSW using the LO (left column in Fig. 15) can detect the centers of the TB and BP, where the extracted images seem to be similar to those for the SO shown previously. However, for the GB, there are several CRSPs offset from the center of the GB. The RPSW using the SO-GS (middle column) succeeds in the detection for the centers of the GB and BP but fails in the detection for the center of the TB. In addition, there is also a mistakenly detected point at the top-right corner for the BP. For the case of LO-GS (right column), the center of the GB cannot be detected well, while the TB and BP can be detected. Thus, the edge extractions by LO, SO-GS, and LO-GS sometimes result in the wrong detections for these targets. We propose that

the SO would be the best operation for the edge extraction for the RPSW.

B. Comparison With Hough Transform

We applied the Hough transform method (HTM) to the same data of the GB, TB, and BP in Fig. 8(d)–(f). In the calculation of the HTM, the maximum and the minimum radii of the circles that we search were set to be 100 and 20 pixels, respectively, which are the same values as those used in the RPSW. We also used the edge extraction before the HTM for the same condition as the RPSW (we also examined the cases without the edge extraction later). Fig. 16 shows that the HTM succeeds in the detection of the circular features of (a) GB and (c) BP, where the center points for the HTM (red “+” symbol) are located at nearly the same point as the maximum CRSP (green circles) for the RPSW (for the case of $s = 5$ in Figs. 9–11). However, the HTM cannot detect the center of the TB, where the center point of the detection deviates from the center of the TB. We also examined the cases without the edge extraction, but we found that the HTM fails to detect the center of the TB.

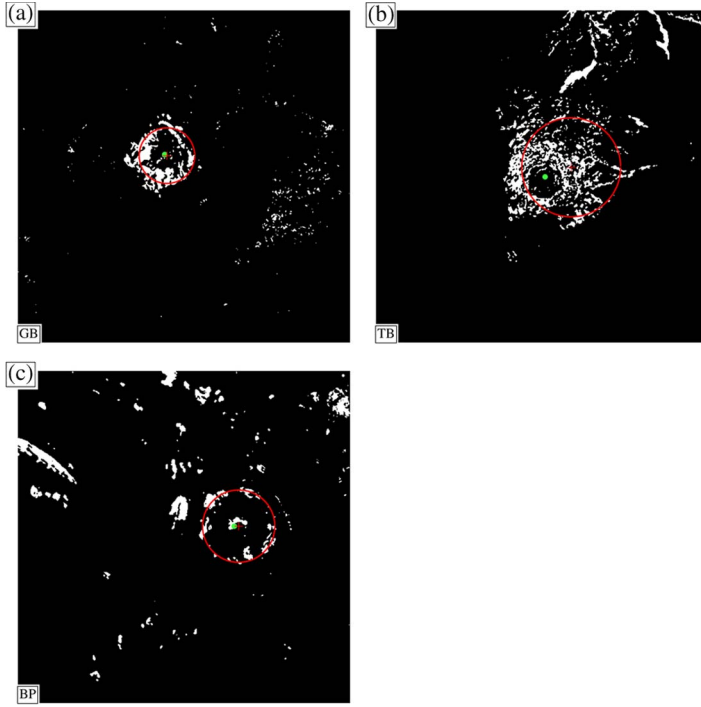


Fig. 16. (Red circles) Detected circles by HTM for (a) GB, (b) TB, and (c) BP. The center point for the detected circle is plotted as red “+” symbol. For a comparison, the maximum CRSP by the RPSW is also plotted as a green filled circle.

Furthermore, we applied both methods to an artificial image of a weak circular feature with a lot of extraneous noncircle features, as shown in Fig. 17(a). Fig. 17(b) shows the result by the RPSW with the parameters in Table II, where the RPSW can detect well the center of the weak circle. On the other hand, Fig. 17(c) shows that the HTM cannot detect the center of the weak circle, where the center point by the HTM deviates from the center of the weak circle. (We also examined the case without the edge extraction, but we found that the HTM fails to detect this weak circle.) It is therefore suggested that the RPSW provides more stable detection for the circular features than the HTM.

On the other hand, there are still weak extraneous features around the circular feature in the extracted image in Fig. 17(b). For an improvement for the extracted image, the combination of the RPSW and HTM would be useful. In this case, we first determine the center of the circular features by the RPSW and then determine the circle (namely, the size of the circle) for the detected circular feature applying the HTM to the limited area around the detected center.

Finally, we compared T between the RPSW and the HTM for the results in Figs. 16 and 17. Table III summarizes T for both cases. The T for the HTM ranges from 514 to 2120 s, while T for the RPSW ranges from $T = 32$ to $T = 132$ s. If we apply the RPSW with $s = 10$, which is less than the maximum detectable s as seen in Section V-A2, $T \sim 8\text{--}9$ s for the GB, TB, and BP. Thus, the values of T for the RPSW are about one or two magnitudes less than those for the HTM.

VI. CONCLUSION

In this paper, we have developed the RPSW to detect circular features. This method consists mainly of two steps: The first is

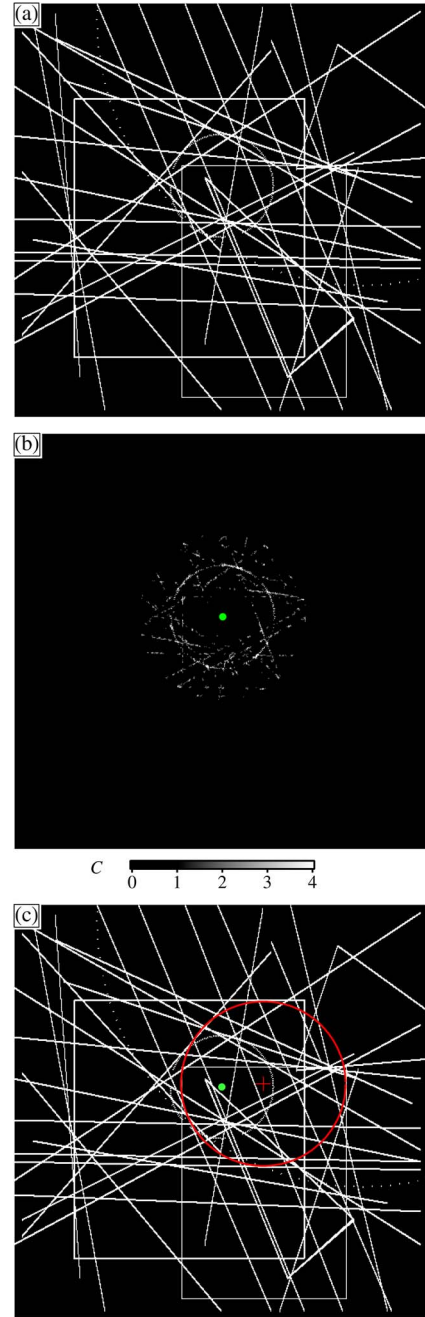


Fig. 17. (a) Artificial pattern with a weak circle on many extraneous non-circle features ($L = 500 \times 500$ pixels). (b) Extracted image of C by the RPSW with a CRSP as a green filled circle ($\Delta\phi = 60^\circ$, $s = 2$, and $f = 0.9$). (c) (Red circle) Detected circle by the HTM with the center point as red “+” symbol. For a comparison, the CRSP by the RPSW is also plotted as a green filled circle.

searching for the CRSPs in a target image, and the second is the extraction of the circular features for the CRSPs. We have shown that the RPSW can detect not only simple circles but also complex circular features such as ring structures, imperfect circles, and concentric circles. We found that the RPSW selectively enhances the RSPs, while the non-RSPs are weakened or eliminated without any noise reduction processes. In addition, we have demonstrated that the RPSW succeeds in the detection of geological circular features (terrestrial impact structures) in binary images based on the ASTER images. We found that

TABLE III
CALCULATION TIME T

Target	RPSW [sec]	HTM [sec]
GB	[†] 32	514
TB	[†] 33	1088
BP	[†] 32	514
Artificial in Fig. 17	132	2120

[†] For the case of $s = 5$.

the optimized parameter for $\Delta\phi$ is $\Delta\phi = 51.4^\circ - 72^\circ$, and the SO is the best operation for the edge extraction as preprocess. In addition, the maximum detectable s depends on the width of the circular feature in a target image. We also found that the RPSW provides more stable detection for the circular features than the HTM. In addition, the calculation time for the RPSW takes one or two magnitudes less than those for the HTM.

Note that the current version of the RPSW cannot be applied to surveys or statistical studies using huge data sets of images obtained by Earth-observation satellites. We need various improvements for such studies. For example, the current version of the RPSW can handle only binary images. When we apply this to multiband or hyperspectral remote sensing images, we have to binarize the multiband or hyperspectral images before applying the RPSW. Therefore, the current RPSW is not a perfectly automatic method. To cope with this issue, we need to change the formulas of R and C . However, this should not be too difficult: What we need to do is to use the rotated image of the multiband or hyperspectral remote sensing images for the calculations of R and C , because the essence of the RPSW is the rotational symmetricalness of the circular features.

The current RPSW gives the plausible centers of the circular features, but we need further evaluation. For example, the RPSW detects the center of the circular features but does not give their sizes. In this case, the combination of the RPSW and HTM would be useful: For example, we first determine the list of the centers of the circular features by the RPSW and then calculate the sizes for each circular feature applying the HTM to the limited area around the center of the circular features.

There is another weak point of the RPSW; RPSW cannot detect the part of a circle or a ring. For example, a quadrant that touches the border cannot be detected by the RPSW, because the quadrant itself is not a rotational symmetrical pattern.

If we apply the RPSW to lunar or planetary images with thousands of circular features per image, further improvement should be needed. In particular, the impact craters in lunar images are characterized by shadows, where the shapes of the impact craters are asymmetric between the sunlight region and the shadow region. Indeed, the previous technique to detect the impact craters uses the asymmetric pattern due to the shadow [7], while the RPSW treats the rotational symmetricalness of a target feature in the image. On the other hand, there is also a series of papers that describe detecting craters from topographic data, e.g., [8] and [9]. Thus, the RPSW would also be applied to topographic data for detecting craters, although we need some preprocesses before applying the RPSW. These improvements will be our future work for the RPSW.

ACKNOWLEDGMENT

The authors would like to thank S. Kato of the National Institute of Advanced Industrial Science and Technology for the technical supports and helpful comments in the analysis of the Advanced Spaceborne Thermal Emission and Reflection Radiometer data.

REFERENCES

- [1] L. Folco *et al.*, "The Kamil Crater in Egypt," *Science*, vol. 329, no. 5993, pp. 804–804, Aug. 2010.
- [2] P. V. C. Hough, "Method and means for recognition complex patterns," U.S. Patent 3 069 654, Dec. 18, 1962.
- [3] J. H. Han, L. T. Koczy, and T. Poston, "Fuzzy Hough transform," *Pattern Recognit. Lett.*, vol. 15, no. 7, pp. 649–658, Jul. 1994.
- [4] H. Taud and J.-F. Parrot, "Detection of circular structures on satellite images," *Int. J. Remote Sens.*, vol. 13, no. 2, pp. 319–335, Apr. 1992.
- [5] M. C. Burl *et al.*, "Automated detection of craters and other geological features," in *Proc. 6th i-SAIRAS*, St. Hubert, QC, Canada, Jun. 2001, pp. 1–8, Canadian Space Agency.
- [6] R. Honda, Y. Iijima, and O. Konishi, "Mining of topographic feature from heterogeneous imagery and its application to lunar craters," in *Progress in Discovery Science, Final Report of the Japanese Discovery Science Project*, vol. 2281. Berlin, Germany: Springer-Verlag, 2002, pp. 395–407.
- [7] Y. Sawabe, T. Matsunaga, and S. Rokugawa, "Automated detection and classification of lunar craters using multiple approaches," *Adv. Space Res.*, vol. 37, no. 1, pp. 21–27, 2006.
- [8] G. Salamunićara and S. Lončarić, "Open framework for objective evaluation of crater detection algorithms with first test-field subsystem based on MOLA data," *Adv. Space Res.*, vol. 42, no. 1, pp. 6–19, Jul. 2008.
- [9] G. Salamunićara and S. Lončarić, "GT-57633 catalogue of Martian impact craters developed for evaluation of crater detection algorithms," *Planet. Space Sci.*, vol. 56, no. 15, pp. 1992–2008, Dec. 2008.
- [10] G. Salamunićara *et al.*, "Test-field for evaluation of laboratory craters using a crater shape-based interpolation crater detection algorithm and comparison with Martian and Lunar impact craters," *Planet. Space Sci.*, vol. 71, no. 1, pp. 106–118, Oct. 2012.
- [11] S. Lončarić, G. Salamunićara, A. Grumpe, and C. Wöhler, "Automatic detection of lunar craters based on topography reconstruction from Chandrayaan-1 M3 imagery," presented at the Lunar Planetary Science Conference, The Woodlands, TX, USA, Mar. 2011, Paper 1454.
- [12] T. F. Stepinski, W. Ding, and R. Vilalta, "Detecting impact craters in planetary images using machine learning," in *Intelligent Data Analysis for Real-Life Applications: Theory and Practice*, R. Magdalena-Benedito *et al.*, Ed. Hershey, PA, USA: IGI Global, Jun. 2012, ch. 8, pp. 146–159.
- [13] P. Pina, J. Saraiva, and T. Barata, "Automatic recognition of aeolian ripples on Mars," presented at the Lunar Planetary Science Conference, The Woodlands, TX, USA, Mar. 2004, Paper 1621.
- [14] J. Iisaka and T. Sakurai-Amano, "An application of pixel swapping technique to remote sensing," presented at the Proceeding Asian Conference Remote Sensing, Singapore, 2000, Paper OPPOO-13.
- [15] Y. Yamaguchi, A. B. Kahle, H. Tsu, T. Kawakami, and M. Pniel, "Overview of Advanced Spaceborne Thermal Emission and Reflection Radiometer (ASTER)," *IEEE Trans. Geosci. Remote Sens.*, vol. 36, no. 4, pp. 1062–1071, Jul. 1998.
- [16] M. Abrams, "The Advanced Spaceborne Thermal Emission and Reflection Radiometer (ASTER): Data products for the high spatial resolution imager on NASA's Terra platform," *Int. J. Remote Sens.*, vol. 21, no. 5, pp. 847–859, Nov. 2000.
- [17] B. Ramachandran, C. O. Justice, and M. J. Abrams, *Land Remote Sensing and Global Environmental Change. NASA's Earth Observing System and the Science of ASTER and MODIS*. New York, NY, USA: Springer-Verlag, 2011, 873 p.
- [18] H. J. Melosh, *Impact Cratering—A Geologic Process*. New York, NY, USA: Oxford Univ. Press, 1989, 245 p.
- [19] M. J. Cintala and R. A. F. Grieve, "Scaling impact melting and crater dimensions: Implications for the lunar cratering record," *Meteorit. Planet. Sci.*, vol. 33, no. 4, pp. 889–912, Feb. 1998.
- [20] P. W. Hodge, *Meteorite Craters and Impact Structures of the Earth*. New York, NY, USA: Cambridge Univ. Press, 1994.
- [21] D. J. Milton *et al.*, "Gosses Bluff impact structure, Australia," *Science*, vol. 175, no. 4027, pp. 1199–1207, Mar. 1972.

- [22] P. Lambert, J. F. McHone, Jr., R. S. Dietz, M. Briedj, and M. Djender, "Impact and impact-like structures in Algeria. Part II—Multi-ringed structures," *Meteoritics*, vol. 16, no. 3, pp. 203–227, Sep. 1981.
- [23] C. Koeberl, "African meteorite impact craters: Characteristics and geological importance," *J. African Earth Sci.*, vol. 18, no. 4, pp. 263–295, Apr. 1994.
- [24] C. Koeberl, W. U. Reimold, and J. Plescia, "BP and oasis impact structures, Libya: Remote sensing and field studies," in *Impact Tectonics*, C. Koeberl and H. Henkel, Eds. Berlin, Germany: Springer-Verlag, 2005.



Satoru Yamamoto received the Ph.D. degree in planetary sciences from Kobe University, Kobe, Japan, in 1999.

He is currently with the Center for Environmental Measurement and Analysis, National Institute for Environmental Studies, Tsukuba, Japan.

Dr. Yamamoto is a member of the Japanese Society of Planetary Sciences, the Astronomical Society of Japan, and the Remote Sensing Society of Japan.



Tsuneo Matsunaga received the Dr.Eng. degree from The University of Tokyo, Tokyo, Japan, in 1997.

He is currently the Head of the Environmental Information Analysis Section, Center for Environmental Measurement and Analysis, National Institute for Environmental Studies (NIES), Tsukuba, Japan. He is also serving as NIES GOSAT-2 Project Team Leader and Principal Investigator of Spectral Profiler instrument on board the Japanese lunar explorer Kaguya.



Ryosuke Nakamura received the Ph.D. degree in planetary sciences from Kobe University, Kobe, Japan, in 1996.

He was a Research Associate with Kobe University from 1996 to 2000 and an Invited Researcher with the Japan Aerospace Exploration Agency from 2000 to 2004. He is currently a Researcher with the Information Technology Research Institute, National Institute of Advanced Industrial Science and Technology, Tsukuba, Japan.

Dr. Nakamura is a member of the Japanese Society of Planetary Sciences and the Astronomical Society of Japan.



Yasuhito Sekine received the Ph.D. (D.Sc.) degree from The University of Tokyo, Tokyo, Japan, in 2006.

He is currently with the Department of Complexity Science and Engineering, University of Tokyo, Kashiwa, Japan. His major research interest is to understand how planets and satellites evolved atmospheres and oceans that are capable of supporting life. In particular, he is interested in the following topics: 1) the origin and evolution of planetary and satellite atmospheres, including Earth, Mars,

and Titan; 2) chemical evolution in solar nebula and planetary atmospheres; 3) hypervelocity impact of asteroids and comets on planets; 4) geochemical analyses of ancient sedimentary rocks to understand the evolution of Earth's atmosphere; and 5) hydrothermal reactions in icy bodies and asteroids in the solar system.



Naru Hirata received the Dr.Sc. degree from the University of Tsukuba, Tsukuba, Japan, in 1998.

He is currently an Associate Professor with the Research Center for Advanced Information Science and Technology, The University of Aizu, Aizu-Wakamatsu, Japan. He is involved in many Japanese planetary exploration missions, including Hayabusa, Kaguya, and Hayabusa 2. His current research interests are planetary impact phenomena, geomorphology, geoinformatics, and related research fields.

Dr. Hirata is a member of the Japanese Society of

Planetary Sciences.



Yasushi Yamaguchi (M'11) received the Dr.Sc. degree in geology from Tohoku University, Sendai, Japan, in 1989.

From 1984 to 1986, he was a Visiting Scientist at Stanford University, Stanford, CA, USA. He is currently a Professor with the Graduate School of Environmental Studies, Nagoya University, Nagoya, Japan. Prior to joining Nagoya University in 1996, he spent 16 years in the Geological Survey of Japan to study geologic remote sensing and natural resource exploration.

Dr. Yamaguchi is a member of the American Society for Photogrammetry and Remote Sensing, American Geophysical Union, and Remote Sensing Society of Japan.